Chapter 2

Computations in spherical geometry

2.1 Introduction*

Solar oscillations possess abundant diagnostic information about the solar interior. Helioseismology is the study of the variations in the internal structure and properties of the dynamics of the sun from measurements of its surface oscillations. Sophisticated observations of these oscillations have led to the inference of the solar structure, the rotation-rate and large-scale dynamics with considerable accuracy. For example, a major result of helioseismology has been the constraint on the solar neutrino flux which led to a re-evaluation of the properties of the neutrino. Helioseismic analyses use the line of sight Doppler velocity of plasma at the solar photosphere. This surface is in continual motion due to the interaction, impact and reflection of millions of wave modes. The primary source of wave generation is the intense turbulence present in the convecting uppermost surface layers. In the sun, detected waves that possess diagnostic value are either surface gravity or acoustic modes. While surface gravity

**The results of this chapter are reproduced from Hanasoge et al. (2006), Hanasoge & Duvall (2006), Hanasoge et al. (2007), and Hanasoge & Duvall (2007). I performed all the simulation work and wrote most of the content; J. Christensen-Dalsgaard helped compute the ADIPACK data, Tom Duvall, Jr. extracted travel times from the simulations and analyzed south-pole data. The ASH profiles were provided by Marc DeRosa.*

modes are constrained to sample only the surface layers, acoustic modes plumb the depths of the solar interior and re-emerge altered by the structure and dynamics of the solar interior. A substantial part of the wave modes that comprise the acoustic wave spectrum travel distances large enough that incorporating sphericity into the model becomes unavoidable.

The first time-distance (Duvall et al., 1993) validation test involving acoustic simulations, of time-distance helioseismology was performed by Jensen et al. (2003), who computed a 3D wavefield in a solar-like atmosphere in the presence of a finite sized sound-speed perturbation. The inverted data recovered the main features of the perturbation but was still quite noisy. Little has been done, however, in the context of the forward problem in spherical domains to complement the extensive inversion analyses applied to data obtained from the Michelson Doppler Imager (MDI) onboard the Solar and Heliospheric Observatory (SOHO), in operation since 1996.

Our objective is to construct a numerical model that allows waves to propagate within a spherically stratified domain, from which the wavefield can be analyzed. The physics of the sun is governed by an enormous dynamic range, with scales stretching from as short as a meter to as long as several million meters. It is not yet computationally feasible to model this plethora of scales and the phenomena associated with them. Consequently, the goal of this effort is not to produce accurate absolute frequencies to compare with the observations. The aim is to design a careful means to perform *differential* studies on the effects of large-scale flows and asphericities, in the context of global and local helioseismology. The expectation is that the helioseismic signatures of the differences in the acoustic wavefield induced by the presence of flows or asphericities are mostly insensitive to the physics we have chosen to discard. Simulations of the wavefield in the presence of large-scale perturbations can be compared with a reference case that corresponds to a computation of the wavefield in the absence of any flows or perturbations. It is important that the forward model be designed to mimic the Sun as closely as possible because data produced from such a model will likely easily lend themselves to interpretation in the context of the solar case. On the other hand, it is equally useful to leave the system simple enough that we are able to understand the individual contributions of various perturbations on helioseismic metrics such as travel times, mode frequencies etc.

The utility of the forward approach cannot be understated, for it paves the way for us to gauge the ability of helio- and astero-seismology to infer the interior properties of the Sun and other stars. In relation to the Sun, we are already investigating the signal to noise properties of deep active regions, holographic far-side signatures of active regions (sunspots and the like), detection of convection and line-of-sight projection anomalies.

In this chapter, we discuss computational techniques and the issues that are encountered in a system where thermodynamic properties such as temperature, pressure, and density are strongly spatially varying. We also present techniques of validation that were used to demonstrate the verity of this computation. The problem is defined in §2, §3 describes the numerical techniques, §4 introduces the reader to wave behavior in a solar like medium, §5 addresses various computational difficulties, §6 discusses methods of validation and in §7, we summarize and draw conclusions.

2.2 The problem definition

We solve the three-dimensional linearized Euler equations of fluid motion in a spherical shell encompassing $0.24 - 1.0004 R_\odot$, expanded around the spherically symmetric background state described by Model S of the sun (Christensen-Dalsgaard et al., 1996). The assumption of linearity is justifiable since acoustic wave velocity amplitudes are much smaller than the background sound speed within the bulk of the computational domain. Because timescales of acoustic propagation are much smaller than the timescale over which large-scale flows or features (of interest to us) change, we assume that the background state is stationary. In the equations that follow, all background quantities are subscripted with a 0, and all other components are fluctuating.

$$\frac{\partial \rho}{\partial t} = -\boldsymbol{\nabla}\boldsymbol{\cdot}(\rho_0 \mathbf{v}) - \boldsymbol{\nabla}\boldsymbol{\cdot}(\rho \mathbf{v}_0), \tag{2.1}$$

$$\begin{aligned}\frac{\partial \mathbf{v}}{\partial t} = & - \boldsymbol{\nabla}(\mathbf{v}_0\cdot\mathbf{v}) - \boldsymbol{\omega}_0\times\mathbf{v} - \mathbf{v}_0\times\boldsymbol{\omega} - \frac{\rho}{\rho_0}\left(\boldsymbol{\nabla}(\frac{1}{2}v_0^2) + \boldsymbol{\omega}_0\times\mathbf{v}_0\right) \\ & - \frac{1}{\rho_0}\boldsymbol{\nabla}p - \frac{\rho}{\rho_0}g\hat{\mathbf{r}} - \Gamma(r)\mathbf{v} + S(r,\theta,\phi,t)\hat{\mathbf{r}}, \end{aligned} \tag{2.2}$$

$$\frac{\partial p}{\partial t} = -\mathbf{v}_0\cdot\boldsymbol{\nabla}p - \mathbf{v}\cdot\boldsymbol{\nabla}p_0 - \Gamma_1 p_0\boldsymbol{\nabla}\cdot\mathbf{v} - \Gamma_1 p\boldsymbol{\nabla}\cdot\mathbf{v}_0, \tag{2.3}$$

$$\Gamma_1 = \left(\frac{\partial \ln p}{\partial \ln \rho}\right)_{ad}. \tag{2.4}$$

Equations (2.1), (2.2), and (2.3) are equations of continuity, momentum and energy respectively. The derivative on the right-hand side of equation (2.4) is evaluated along an adiabatic process curve (as denoted by the subscript 'ad'). The nomenclature is as follows: ρ is the density, p the pressure, $\boldsymbol{\omega}$ the vorticity, $\Gamma_1 = \Gamma_1(r)$ is the first adiabatic exponent, g is gravity, and $\mathbf{v}$ is the vector velocity. Equation (2.3), which states that wave propagation is adiabatic, is justified because the viscous and heat transfer timescales are long in comparison to the acoustic timescales, over much of the computational domain.

The term $\Gamma(r)\mathbf{v}$ in equation (2.2) plays the role of a damping agent and $S(r,\theta,\phi)\hat{\mathbf{r}}$ is the radially directed dipole source. It is believed that wave excitation in the sun occurs in an extremely narrow spherical envelope (200 km thick) bounded by the surface (e.g., Skartlien & Rast, 1999), and we assume therefore, $S(r,\theta,\phi,t) = \tilde{S}(\theta,\phi,t)\delta(r-r_{ex})$, where $r_{ex} = 0.9997R_\odot$ was chosen to be the radial location of the source. $\tilde{S}$ is a spatially broadband random function for all but the largest horizontal wavenumbers, which are not included so as to avoid any issues of spatial aliasing. The solar wave power spectrum possesses maximum power in the range $2000-5500\mu$Hz with a peak in power around 3200 μHz. In order to mimic this excitation behavior, we generate a Gaussian distributed power spectrum with a mean of 3200 μHz and a standard deviation of 1000 μHz in frequency space, which we then Fourier transform to produce a time series with the appropriate source spectrum.

In this study, we perform simulations over a time period that exceeds the time at which the acoustic energy reaches a statistical steady state. The other requirement for the temporal length of the simulation is that the frequency resolution be sufficient for the application at hand. The velocity time series, extracted at the surface, is projected onto a line of sight and used as artificial Doppler velocity data.

2.3 Numerical method

The procedure we employ is pseudo-spectral; we use a spherical-harmonic representation of the spherical surface, sixth-order compact finite differences in the radial direction (see Lele, 1992) and a second-order, five-stage Low Dissipation and Dispersion Runge-Kutta (LDDRK) time-stepping scheme (see Hu et al., 1996). Latitudes are Gaussian collocation points and longitudes are equidistant. The radial grid is mostly based on the sound speed distribution and is discussed further in § 5.1. The code was developed and run on a multiprocessor SGI-Altix machine at Stanford.

2.3.1 Parallelism in OpenMP

One of the parallel implementations is in OpenMP (shared memory) with radial locations domain distributed, allowing all the spherical-harmonic transforms to be performed in-processor. Spherical-harmonic transforms are computed in two steps: longitudinal FFTs at each latitude and radius followed by Legendre transforms for each Fourier coefficient and radius. FFTs are performed using the Guru routines provided in FFTW 3.0 and Legendre transforms using matrix-matrix multiplication techniques implemented in Level 3 Basic Linear Algebra Subroutines (BLAS). The associated Legendre polynomials P_l^m, where l and m are the spherical-harmonic degree and order respectively, are divided into a series of matrices corresponding to different m's, each of which is further divided into two matrices according to whether $(l - m)$ is even or not. This is done to exploit the symmetry of the associated Legendre polynomials about the equator, which speeds up the transform by a significant amount.

The associated Legendre polynomials are computed according to a highly stable four term recurrence algorithm given by Belousov (1962), available at netlib (the STSWM package). Each transform is a computation of order $O(n_{lon}^2 \cdot n_{lat} \cdot n_{rad} \cdot \log(n_{lon}))$, where n_{lon} is the number of longitudinal gridpoints, n_{lat} the number of latitudinal gridpoints and n_{rad} the number of radial gridpoints. To prevent aliasing, we apply the two-thirds rule (Orszag, 1970) which sets the lower bound on the number of latitudes at $3l_{max}/2$ where l_{max} is the maximum l of the simulation. To ensure equal resolution in the latitudinal and longitudinal directions, we set $n_{lon} = 2n_{lat}$. Recasting the minimum operation count in term of l_{max}, we obtain an expensive operation count of $O(n_{rad} \cdot l_{max}^3)$; it is therefore important to minimize the number of times spherical-harmonic transforms are performed. Every timestep requires the computation of a curl, divergence, and four gradients, each of which involves a computational equivalent of a forward-inverse transform pair. Level 3 BLAS is known to operate near the peak performance of the processor, so these computations are generally very efficient, when they are performed in-processor.

2.3.2 Parallelism according to message passing

The code was re-written according to the Message Passing Interface (MPI) standard, a version that runs well on large numbers of processors, and at large values of l, as opposed to the OpenMP version, which does not do quiet so well on large problems. In the MPI version, data is domain distributed according to latitudes in real space, and Fourier coefficients in Fourier space. Spherical-harmonic transforms are computed in two steps:

1. Longitudinal FFTs at each radius (all located in-processor) and the in-processor latitudes.

2. The data is transposed and redistributed across processors, so that all latitudes and radial points corresponding to a Fourier coefficient are in-processor. This is to ensure that the Legendre transforms for each Fourier coefficient and radius are computed optimally.

The FFTs and Legendre transform are implemented in the same manner as described in §2.3.1. Spherical harmonic coefficients are divided across processors using the algorithm described by Foster & Worley (1997).

We place transmitting boundary conditions (Thompson, 1990) at both radial boundaries of the computational domain. While this particular boundary condition is most effective at absorbing waves that are of normal incidence, it reflects a significant percentage of all other waves. To mitigate this effect, we introduce an absorbent buffer zone (for example, see Lui, 2003; Colonius & Lele, 2004), placed in the evanescent region, that damps waves out substantially before they reach the boundary. This is one of the purposes that the term $\Gamma(r)$ in equation (2.2) fulfils.

2.4 Acoustic wave propagation in the sun

Acoustic modes are uniquely identified by three parameters, the spherical-harmonic degree l, azimuthal order m, and radial order n. A detailed description of this classification system and more on wave behavior as a function of these parameters can be found in chap. 5 of Christensen-Dalsgaard (2003). Because sound speed increases with depth, waves that are initially propagating at a non-zero angle to the upper boundary refract continually as they propagate deeper until they undergo total internal refraction at some depth and re-emerge at the surface. At the point of total internal refraction, also known as the inner turning point, the wave is propagating purely horizontally. To determine the location of the inner turning point we proceed as follows. The dispersion relation is

$$\omega = ck, \tag{2.5}$$

where ω is the frequency, c the sound speed, and $k = |\mathbf{k}|$, where $\mathbf{k}$ is the vector wavenumber. We decompose $\mathbf{k}$ into a radial ($k_r\hat{\mathbf{r}}$) and a horizontal ($\mathbf{k_h}$) component according to

$$\mathbf{k} = k_r\hat{\mathbf{r}} + \mathbf{k_h}. \tag{2.6}$$

We have, using equations (2.5) and (2.6),

$$k_r^2 + k_h^2 = \frac{\omega^2}{c^2}, \tag{2.7}$$

where $k_h = |\mathbf{k_h}|$, the horizontal wavenumber, is given by

$$k_h(r) = \frac{\sqrt{l(l+1)}}{r}. \tag{2.8}$$

To determine the inner turning point, r_t, we set $k_r = 0$, and obtain

$$\frac{c(r_t)}{r_t} = \frac{\omega}{\sqrt{l(l+1)}}. \tag{2.9}$$

This relation thus provides us a means to identify the maximum penetration depth of each wave mode. The inverse is true as well: the frequency-wavenumber range of waves that can access a given depth may be determined from equation (2.9).

2.4.1 Upper turning point: reflection at the surface

The acoustic cutoff frequency ω_A, below which waves become evanescent, is related to the density scale height, H_ρ, in the following manner (Deubner & Gough, 1984)

$$\omega_A = \frac{c}{2H_\rho}\left(1 - 2\frac{dH_\rho}{dr}\right)^{\frac{1}{2}}. \tag{2.10}$$

We define H_ρ as

$$H_\rho = -\left(\frac{d\ln\rho}{dr}\right)^{-1}, \tag{2.11}$$

and in a similar manner, the pressure scale height, H_p, as

$$H_p = -\left(\frac{d\ln p}{dr}\right)^{-1}. \tag{2.12}$$

As waves propagate towards the surface, the density and pressure scale heights become increasingly small, as depicted in Figure 2.1. The dependence of the cutoff frequency as a function of radius is shown in Figure 2.2. Waves possessing frequencies higher than 5500 μHz or so escape into the atmospheric layers and they are of little interest to us. The rest of the spectrum is reflected at locations, also known as the upper turning points, where the wave frequency equals the cutoff frequency. This property was taken into account when choosing the excitation parameters. A useful consequence of this arrangement is that above their upper turning points, waves with frequencies less than the cutoff become evanescent. This aids the design of a transparent boundary condition, since these waves can be damped into non-existence much more easily.

2.5 Computational issues

Computationally speaking, the properties of the sun are relatively well behaved and comparatively easy to model up to about $r = 0.98R_\odot$. The near-surface layers however, introduce the multiple difficulties of rapidly dropping density height scales, increasingly unstable stratification, the presence of an ionization zone, complexity in the equation of state, and nonlinearities into the wave propagation physics. Added to these issues is the fact that acoustic waves spend most of their time in the near-surface layers because the sound speed is smallest here. The consequences of not taking into account some or all of the complex near-surface dynamics is not entirely clear because the issues listed above are inextricably linked to each other.

Keeping in mind the important issue of computational feasibility, we cannot hope to resolve the complex small-scale physics of the near-surface layers or model the convecting solar interior. In fact, we see the formalism presented in this article as complementary to the work of, e.g., Rosenthal et al. (1999), Georgobiani et al. (2003), who perform detailed hydrodynamical simulations of the near-surface layers to extract information about their effects on the frequencies and excitation of the modes. We reiterate that the method presented herein is a means to study the *differential* effects of flows and asphericities on various helioseismic measures, such as resonant frequencies, travel-time anomalies etc..

2.5.1 Choice of radial grid

To determine an appropriate radial grid, we have taken into account the strong radial dependence of background solar properties such as pressure, density and sound speed. Consider a wave propagating at the speed of sound in the radial direction according

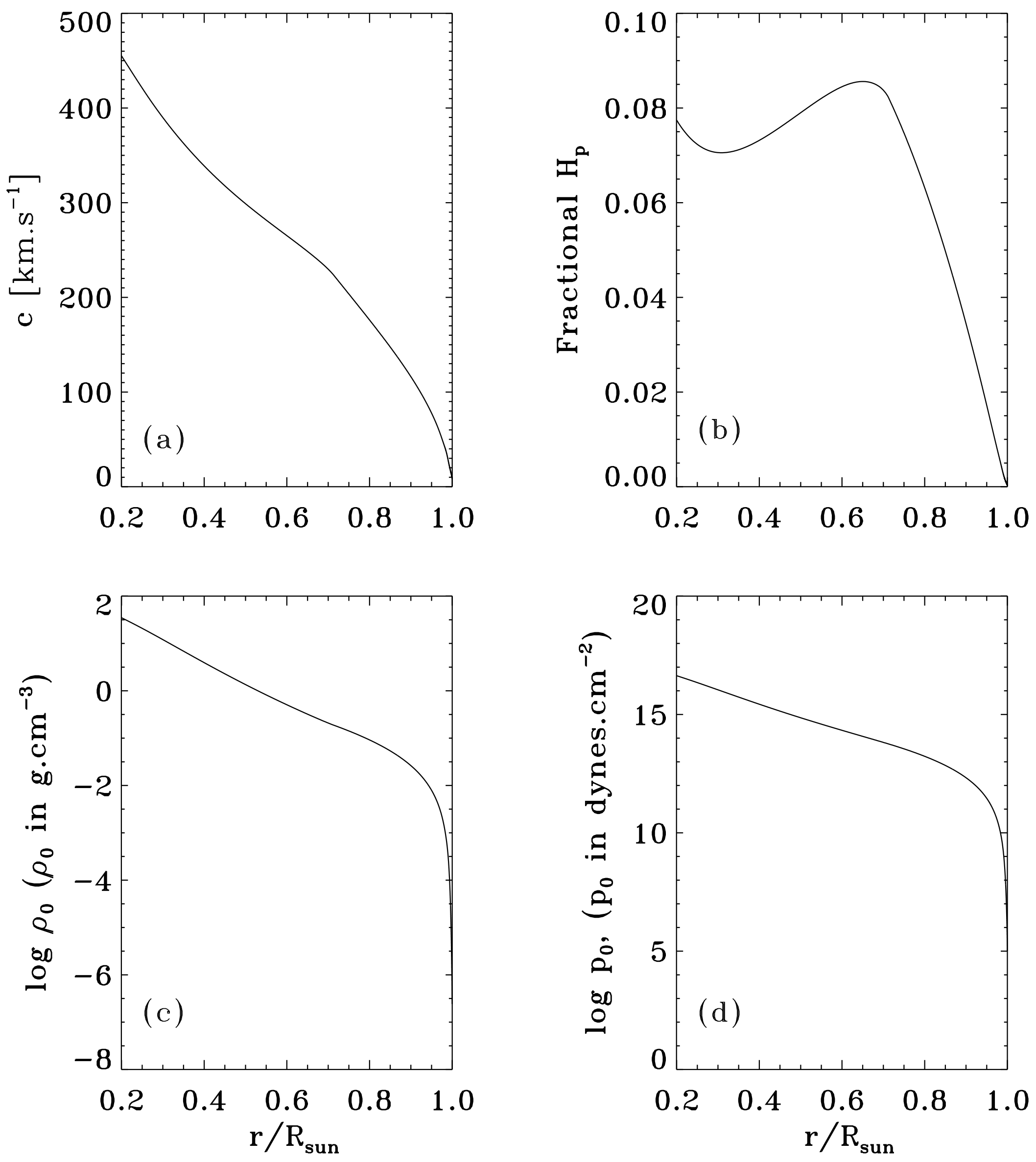

Figure 2.1 Background properties from model S of the sun (Christensen-Dalsgaard et al., 1996) as functions of radius. The horizontal coordinate of all the panels above is the fractional radius, $r/R_\odot$. Panel (a) shows the dependence of sound speed (in $\mathrm{km}\cdot\mathrm{s}^{-1}$) with $r/R_\odot$. Panel (b) contains the fractional pressure scale height variation ($H_p/R_\odot$; H_p has been defined in Eq. [2.12]) with the fractional radius. Note the rapidly decreasing scale height in the near-surface layers. Panel (c) and (d) show logarithmic variations in density and pressure as a function of the fractional radius.

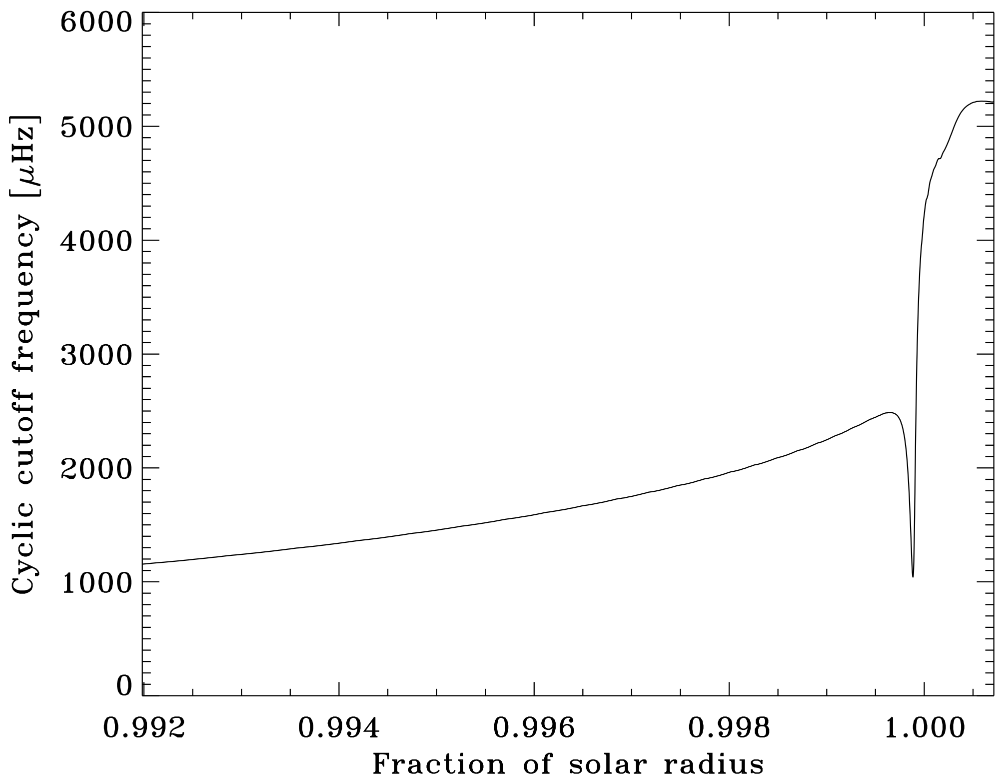

Figure 2.2 Acoustic cutoff frequency $\omega_A/2\pi$ as a function of radius in the model. The steep rise in ω_A in the near-surface layers is due to rapid changes in the density scale height, and causes outward-propagating waves with frequencies $\omega < \omega_A$ to reflect and propagate inward.

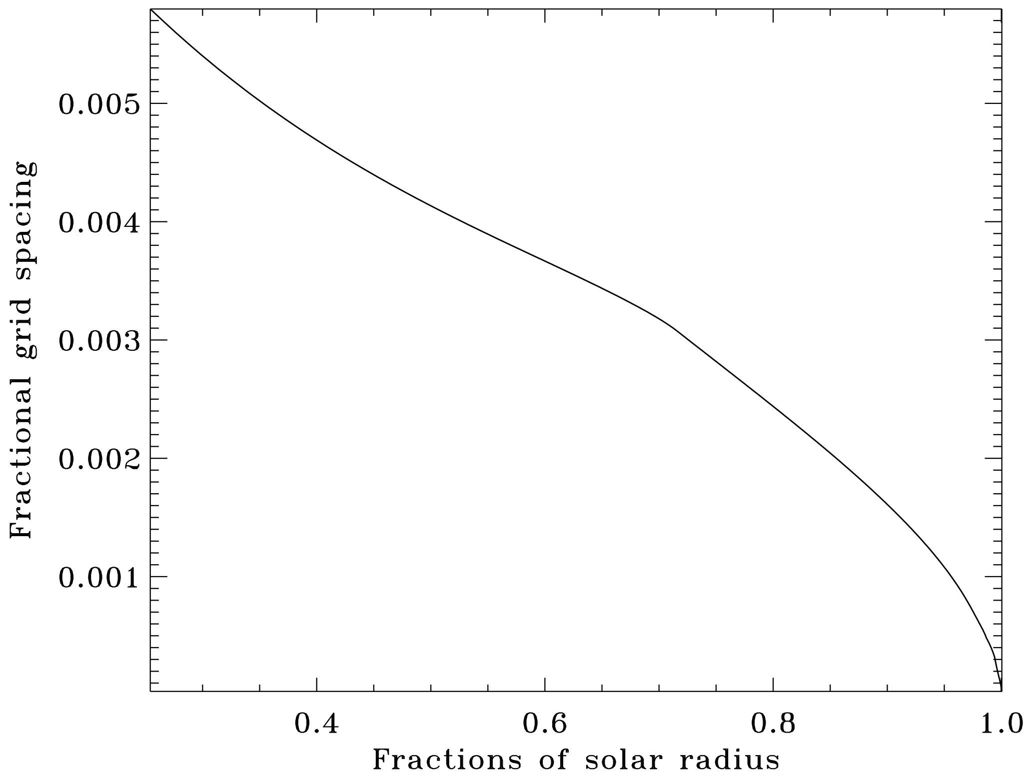

Figure 2.3 Fractional grid spacing as a function of radius for $n_{rad} = 350$. Plotted is $dr/R_\odot$, where dr is the local grid spacing, as a function of the fractional radius, $r/R_\odot$. For $r \leq 0.99R_\odot$, the grid spacing is chosen to maintain the constancy of the travel time of an acoustic wave between adjacent grid points. To account for rapidly decreasing scale heights, the radial grid points from $0.9915R_\odot$ to the upper boundary are equally spaced in $\ln p$. Third order splines are used to vary the grid spacing between 0.99 and $0.9915R_\odot$ as smoothly as possible.

to the simple advection equation

$$\frac{\partial u}{\partial t} + c(r)\frac{\partial u}{\partial r} = 0. \tag{2.13}$$

It makes immediate sense to choose a grid stretching function

$$\tau(r) = \int_r \frac{dx}{c(x)}, \tag{2.14}$$

that transforms equation (2.13) to

$$\frac{\partial u}{\partial t} + \frac{\partial u}{\partial \tau} = 0, \tag{2.15}$$

a form that is much easier to handle. The relation between two adjacent grid points then is

$$\int_{r_i}^{r_{i+1}} \frac{dr}{c} = \delta, \tag{2.16}$$

$$\delta = \frac{1}{n_{rad} - 1}\int_{r_{in}}^{r_{out}} \frac{dr}{c}, \tag{2.17}$$

where r_{in}, r_{out} are the inner and outer radii respectively and n_{rad} is the number of radial grid points including the boundaries. Since sound speed is a monotonically decreasing function of radius, the radial grid spacing becomes larger at depth. Also important to note is that gradients of background quantities become smaller with depth and it makes sense that the grid is coarser.

However, as noted in §4, pressure and density scale heights tend to become very small at the surface and pressure and density fall much more rapidly with radius than sound speed. It is therefore useful to choose a different heuristic for the grid spacing for the outer layers, perhaps along the lines of a logarithmic pressure grid. In this simulation, we have adopted a constant travel-time grid for $r \leq 0.99R_\odot$, patched smoothly with one equally spaced in $\ln p$ from $0.9915R_\odot$ to the upper boundary. Third order splines are used to vary the grad spacing between 0.99 and $0.9915R_\odot$ as smoothly as possible. Figure 2.3 displays the grid spacing as a function of radius.

2.5.2 Spectral blocking and radial dealiasing

Spectral blocking is an aliasing phenomenon that commonly occurs in non-linear calculations, wherein the lack of resolution results in a super-linear accumulation of energy near the Nyquist frequency. It poses a serious numerical challenge, since the energy growth is very rapid, leaving the computation unstable and inaccurate. We discuss its appearance in our *linear* calculations and how we deal with this issue. Standard Fourier transforms are defined on grids where the travel time for waves between adjacent grid points is a constant over the grid. In the solar case, the sound speed is a strong function of radius and consequently, it makes little sense to speak of a Fourier transform on a uniformly spaced radial grid. The Fourier transform in this situation is only made meaningful on a grid stretched such that the travel time between adjacent grid-points is constant over the grid. The rest of the discussion in this section follows as a consequence of this grid stretching and the consequent interpretation of the Fourier transform on this grid.

As described above, the source function is highly limited in the radial direction resulting in the excitation of waves with a wide spectrum of radial orders. The resolution in the radial direction is restricted by the finiteness of computational resources at our disposal and the scientific interest in investigating these high radial orders. For the applications that we are interested in, both these criteria indicate that these high radial orders are best done away with. Associated with the inability of the radial grid to capture modes containing rapid variations is the phenomenon of aliasing which causes waves beyond the resolvable limit of the grid to fold back across the Nyquist onto the resolvable waves near the Nyquist. This by itself is not a serious problem since we are only interested in a small number of ridges that are situated well away from the radial Nyquist. Typically, aliasing in linear problems is relatively harmless and usually only results in a slight increase in power near the Nyquist.

Interestingly however, in our calculations, Fourier transforms in the radial direction display spectral blocking (shown in figure 2.4), an effect that occurs in numerical solutions of non-linear equations, commonly seen in simulations of turbulence and other non-linear phenomena. It is seen in our computations because of the highly non-constant terms (in the solar case) of the Euler equations, density, pressure and sound speed, that pre-multiply the linear fluctuation terms, like the first term on the right-hand-side of equation (2.1). These non-constant terms act as conveyor belts across the radial spectrum, transferring energy between disparate wavenumbers, and eventually cause this aphysical energy build-up at the Nyquist. The energy accumulation occurs at a non-linear rate, rapidly posing a threat to the accuracy and stability of the calculation.

In order to dealias the variables, we apply the 11 point de-aliasing filter (Vichnevetsky & Bowles 1982) given in equation [2.18], where $\hat{u}_n$ and u_n are the filtered and unfiltered variables at grid point n, every few time-steps so that any growth near the Nyquist is suppressed. Because of the high order of the filter, the portion of radial spectrum of interest is left largely unaffected. Note that because of the varying sound speed, we can only apply the filter on the stretched grid over which the acoustic travel time between adjacent grid points is constant.

$$\begin{aligned}
\hat{u}_n &= a_0 u_n + \frac{a_1}{2}(u_{n-1} + u_{n+1}) + \frac{a_1}{2}(u_{n-2} + u_{n+2}) \\
&+ \frac{a_2}{2}(u_{n-2} + u_{n+2}) + \frac{a_3}{2}(u_{n-3} + u_{n+3}) \\
&+ \frac{a_4}{2}(u_{n-4} + u_{n+4}) + \frac{a_5}{2}(u_{n-5} + u_{n+5}) \qquad (2.18) \\
a_0 &= 0.753906,\ a_1 = 0.410155,\ a_2 = -0.234375, \\
a_3 &= 0.087890,\ a_4 = -0.019531,\ a_5 = 0.001953
\end{aligned}$$

2.5.3 CFL restrictions

The Courant-Friedrich-Lewy (CFL) condition determines the maximum size of the timestep based on spatial resolution and, in this case, sound speed. The timestep is limited by the more restrictive of the accuracy and stability conditions (see Hu et al., 1996). The accuracy condition requires that well resolved waves are captured to within accepted numerical error and the stability condition ensures that the highest resolved wavenumber is stable. Since waves travel at various angles, we must consider limitations due to the horizontal wavenumber as well.

The shortest wavelength that can be accommodated on the radial grid (without

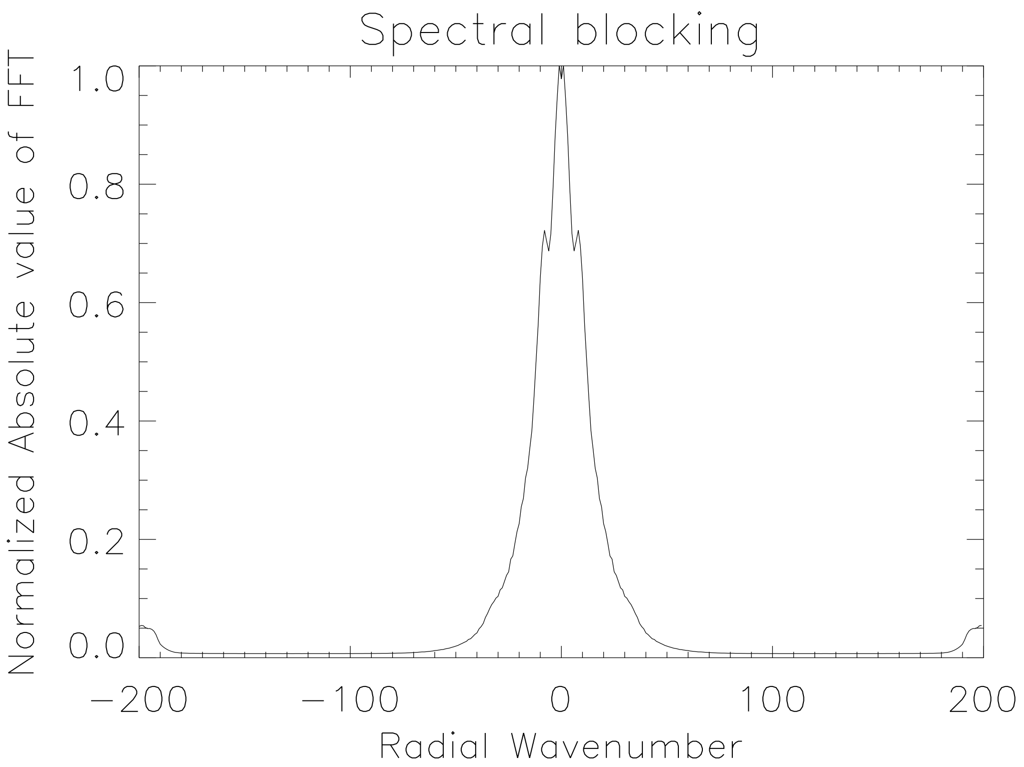

Figure 2.4 Spectral blocking in a linear simulation. This is a classic malaise affecting non-linear calculations, resulting in aphysical energy accumulation near and at the Nyquist. Although the amplitude at the spatial Nyquist (either end of the graph) is relatively small in this snapshot, the time evolution of this region of the spectrum is nonlinear.

any aliasing) is twice the largest grid spacing, which is the distance between the deepest two grid points. Since the spatial differencing scheme can only capture derivatives with wavenumbers in a given range, we introduce two relevant measures (e.g., Lele, 1992; Lui, 2003) used to describe this effect: the highest well-resolved wavenumber and the highest resolved wavenumber. The highest well-resolved wavenumber represents the largest wavenumber which is resolved accurately by the differencing scheme. The highest resolved wavenumber is the maximum effective wavenumber of the spatial differencing scheme. The highest well-resolved radial wavenumber, which we refer to as k_w, and highest resolved radial wavenumber, k_{wn} for the choice of our differencing scheme are $k_w h = 1.7$ and $k_{wn} h = 2.0$, where h is the local radial grid spacing. The highest well-resolved horizontal wavenumber (for a spectral method, there is no difference between the highest resolved and highest well-resolved wavenumbers) is given by

$$k_{h,max} = \frac{\sqrt{l_{max}(l_{max}+1)}}{r_{in}}, \tag{2.19}$$

where l_{max} is the spherical-harmonic bandwidth. The timestep restriction is given by

$$\Delta t \leq \min\left[\frac{L}{(ck_w)_{max}}, \frac{R}{(ck_{wn})_{max}}, \frac{L}{(ck_h)_{max}}\right], \tag{2.20}$$

where R and L are limited by the boundary of the stability foot-print and the accuracy limit respectively (Hu et al., 1996). The time-stepping scheme adopted in this calculation is accurate and stable for $L \leq 1.35$ and $R \leq 3.54$, and therefore the largest allowed timestep is given by

$$\Delta t = \min\left[1.67\left(\frac{h}{c}\right)_{min}, \frac{1.35}{\sqrt{l_{max}(l_{max}+1)}}\frac{r_{in}}{c_{max}}\right], \tag{2.21}$$

where h and c are functions of radius and $c_{max} = c(r_{in})$ is the maximum sound speed in the domain. In practice, we have succeeded in using larger timesteps than that allowed by the CFL condition; in most simulations, we use $\Delta t = 4$ seconds.

2.5.4 Lower boundary issues

Pushing the lower boundary deep (like $0.24R_\odot$) is certain to ensure a tight CFL restriction, especially if there is a horizontal background structure (like a density inhomogeneity or a flow) that interacts with the acoustics. Consider equations (2.19) and (2.20) - as one proceeds deeper, the inner radius r_{in} reduces and sound speed (see Figure 2.1) increases. The timestep restriction becomes tighter and consequently the computation becomes very expensive. We have therefore actively made the choice of a spherically symmetric background model with no flows at this depth. Consider also the fact that a large number of waves have already undergone total internal refraction. For example, at a frequency of 5000 μHz, the highest l that penetrates a depth of 0.24 $R_\odot$ is 10, which means that when determining the CFL condition from equation (2.21), one need not use the entire spherical bandwidth. In other words, one may replace l_{max} by $l_{max}(r)$ denoting the highest l that can propagate at a given radius (given by Eq. [2.9]), a number which deep in the sun is much smaller than the bandwidth. The resulting time-step increase one can obtain by applying this property can be as large as a factor of 2 depending on l_{max} and the number of radial gridpoints.

2.5.5 Buffer layer

It was mentioned in §2.3 that the transmitting boundary conditions employed in this calculation reflect a large percentage of waves that impact it at significant angles (as opposed to purely radially propagating waves). The effect poses a serious threat to both the stability and accuracy of the simulation because of this aphysical reflection of waves. To deal with this problem, we insert a buffer layer adjoining the upper boundary in which upward traveling waves are significantly damped out prior to reaching the upper boundary. This ensures that even if these waves are reflected at the boundary, they will have to propagate through the buffer layer again to reach the computational region of interest. This layer serves to diminish the amplitudes of these aphysical waves to insignificance. Thus, in order to prevent unwanted reflections, we introduce buffer layers at each end of the computational domain via the damping term $\Gamma(r)\mathbf{v}$ in equation (2.2).

One problem associated with using such a lower boundary buffer layer is in dealing with waves that have inner turning points located in the midst of the buffer zone. These waves essentially sample the buffer zone and undergo a total internal reflection only to re-emerge corrupted by this aphysical layer. The task then is to identify and filter out these waves. As explained in §2.4 and specifically in equation (2.9), we can identify the frequency-wavenumber range of waves which propagate to this depth and nullify the corresponding part of the $k - \omega$ spectrum.

2.5.6 Convective instabilities

The Brunt-Väisälä frequency indicates whether a medium is unstable to convection. It is given by (e.g., Christensen-Dalsgaard, 2003, chap. 3)

$$N^2 = g\left(\frac{1}{\Gamma_1}\frac{\partial \ln p}{\partial r} - \frac{\partial \ln \rho}{\partial r}\right), \tag{2.22}$$

where g is gravity, N is the Brunt-Väisälä frequency and Γ_1 is the first adiabatic exponent, defined in equation (2.4). The solar convection zone extends all the way from roughly $0.7R_\odot$ to the surface. For purposes of discussion, we shall divide the convection zone into two regions, $0.7R_\odot < r < 0.996R_\odot$ where timescales of convective growth are considerably larger than acoustic timescales (5 minutes) and $0.996R_\odot < r < 1.0003R_\odot$ where the convective growth rate and acoustic timescales are about equal. Consider the inner region with slowly growing instabilities first. Since we are dealing with a linear system, it might at first sight seem odd that although we restrict acoustic excitation to the bandwidth $2000-5500$ μHz, we still see instabilities at much lower frequencies. The reasons for this are the finiteness of the excitation time series, which results in the broadening of the frequency response, and numerical round-off errors, which act as broadband sources.

The outer convective envelope introduces difficulties which must be treated with greater care. As can be seen in Figure 2.5, the instability time-scales very close to the surface coincide with the center of the acoustic bandwidth. Since our interest lies in capturing the interaction of the acoustics with the background dynamics and not in the direct computation of the convection, we must devise a means to remove this

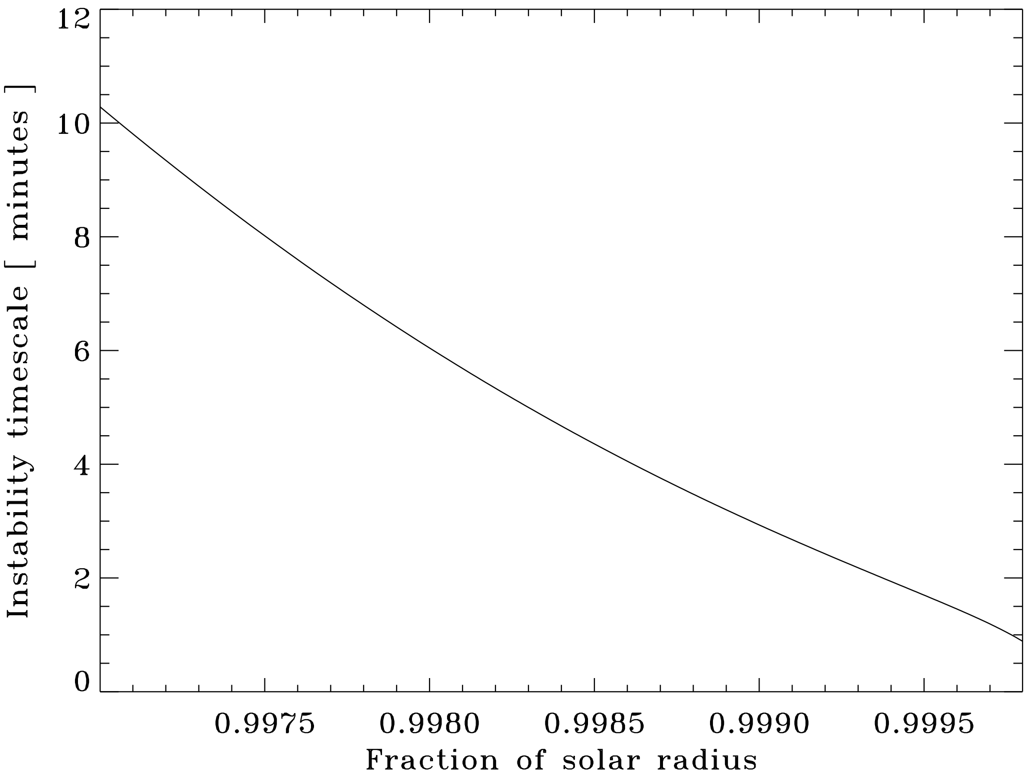

Figure 2.5 Convective instability timescales, ($1/|N|$ in minutes) as a function of the non-dimensional radius. It can be seen that growth rates of the convective instabilities lie in the same range as the time-scales associated with the acoustic waves. The instability arises as a direct consequence of the super-adiabaticity of the background model, and since we are not modeling the nonlinear physics of convection, it is crucial that we prevent this linear instability (described in §2.5.6) from affecting the acoustic signal.

instability without affecting the acoustics. One way to accomplish this is to alter the Brunt-Väisälä frequencies. A crucial requirement is that the acoustic impedance of the surface layers not be changed by much, since all the acoustic reflection occurs in and around these layers.

It is difficult to alter the timescales of convective growth in the near-surface layers of model S without rendering the background model inconsistent. We have therefore replaced the near-surface layers given by model S, more specifically, the region above $0.98R_{\odot}$, with an alternative empirical description that satisfies requirements of hydrostatic consistency, convective stability and preserves the crucial reflective property of the solar atmosphere. Equally essential is that the atmosphere be a smooth extension to the interior (given by model S). Some properties of the empirical model are shown in Figures 2.6 and 2.7 and listed in appendix A; more details may be found in Hanasoge (2006). It should be noted that this modification of the background model allows the temporal window of the simulation to be extended to several days; longer simulations, of the order of weeks, are still susceptible to the marginal super-adiabaticity exhibited by the interior.

2.6 Validation

An important indicator of solar wave structure (acoustic, surface-gravity) is the power spectrum, which embodies the frequency-wavenumber response of the system to a specific excitation. It is typically shown as the squared Doppler velocity as a function of ω and l. In other words, it is the frequency-wavenumber response of the system to a specific excitation. It can also be understood as a depiction of the resonant modes of the model. A mixture of surface-gravity and acoustic modes appear when solar surface (Doppler) velocities are analyzed. As stated before, the acoustic modes possess maximum power in the frequency range of $2000-5500$ μHz. In terms of spatial wavenumbers, the solar power spectrum stretches to extremely high harmonic orders (several thousand) which are at present computationally infeasible. The immediate aim is to replicate some part the low to medium-l ($0 < l < 400$) acoustic spectrum of the sun in the frequency range described above. We achieve this by exciting waves only

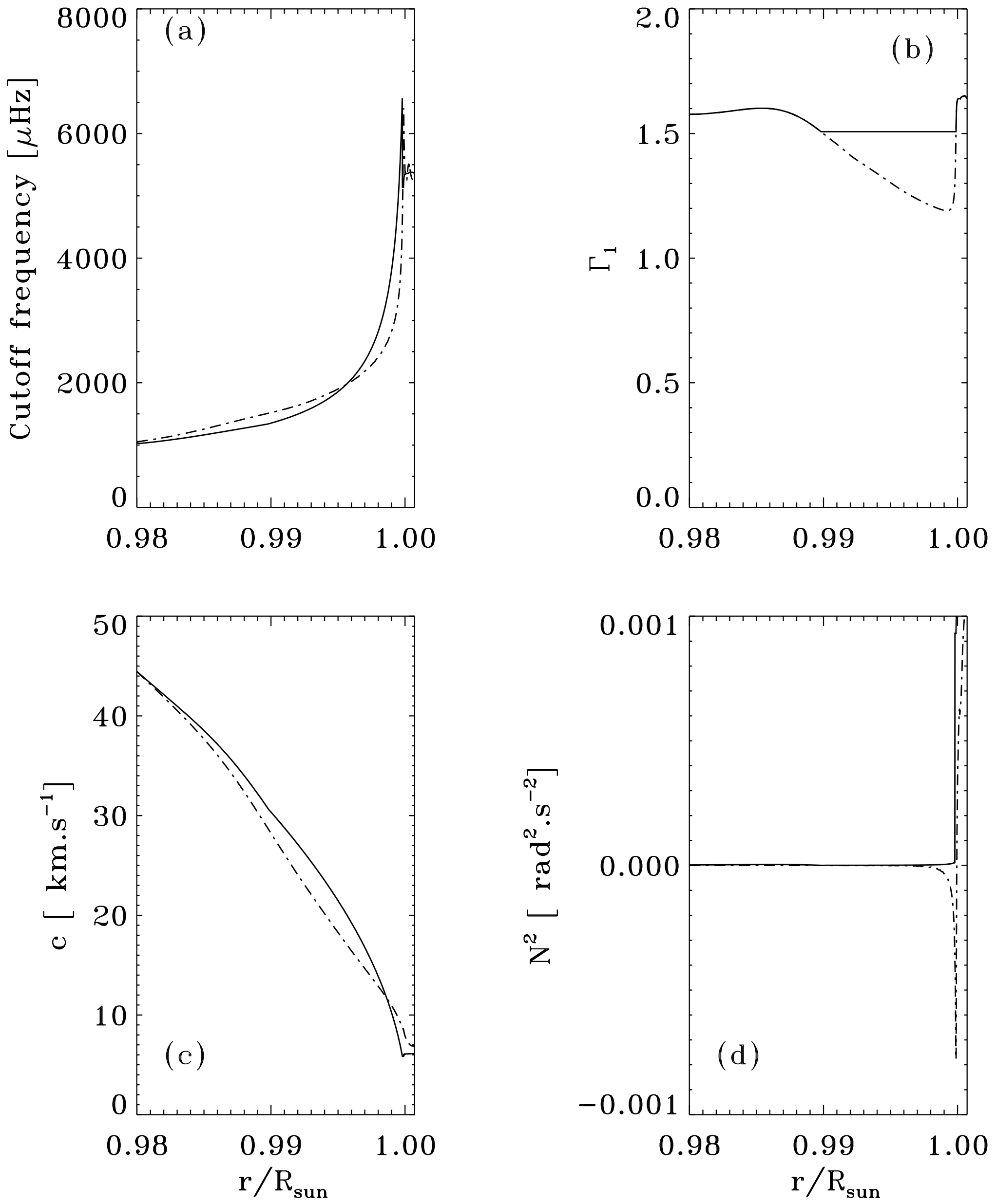

Figure 2.6 These panels show a comparison between the properties of the atmosphere given by model S (dot-dash line) and the artificial model (solid line) used in the computation. The horizontal coordinate of all the above panels is the fractional radius, $r/R_{\odot}$. Panel (a) shows the cutoff frequency dependence with radius; the reflective property of model S is recovered quite accurately by the artificial model. Panel (b) is a comparison of the first adiabatic exponents; Γ_1 has been altered to render the artificial atmosphere convectively stable. Panel (c) shows sound speed dependence with radius; the layer extending from $0.9998R_{\odot} \leq r \leq 1.0007R_{\odot}$ is isothermal and therefore the sound speed is constant in that region. Panel (d) displays the all-important measure of convective stability, the Brunt-Väisälä frequency; it can be seen that the artificial model is sub-adiabatic in the near surface layer, thus ensuring the convective stability of the outer layers.

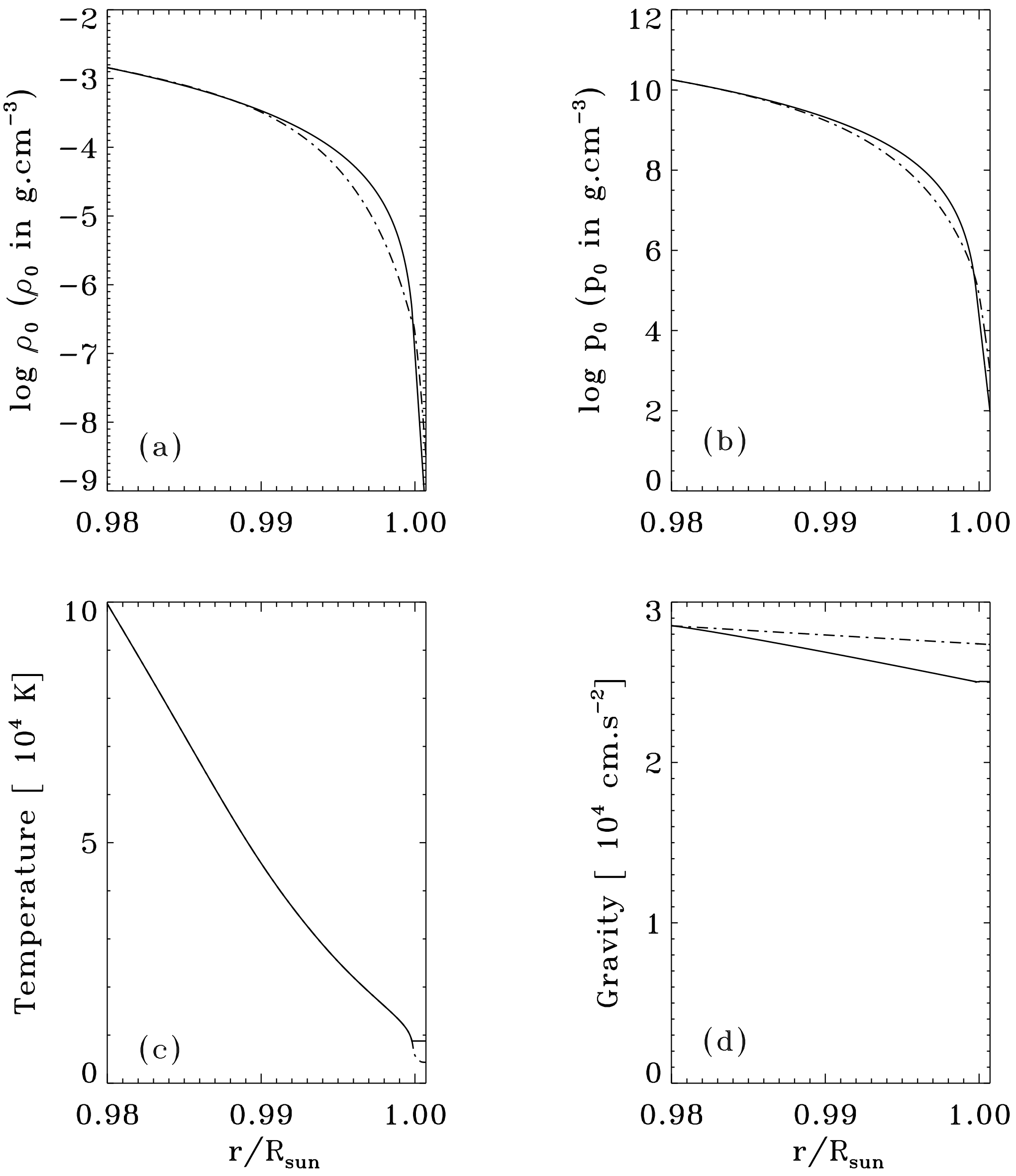

Figure 2.7 These panels show a comparison between the properties of the atmosphere given by model S (dot-dash line) and the artificial model (solid line) used in the computation. The horizontal coordinate of all the above panels is the fractional radius, $r/R_{\odot}$. Panels (a) and (b) show the variation of the logarithmic density and pressure with radius; it can be seen that the two models are quite similar. Panel (c) is a comparison between temperature profiles - the isothermal nature of the outermost layers of the artificial model is visible. Panel (d) shows gravity dependence with radius; the gravity profile of the artificial model is seen to decay more rapidly than that of model S.

in the specified frequency band. Figure 2.8 is the log power spectrum obtained from a 24 hour long simulation with transmitting lower and upper boundaries placed at $0.24R_\odot$ and $1.0002R_\odot$ respectively. Note that because the short time-scale convective instabilities present in the atmospheric region of the background model have been removed, we see no power at frequencies below 2000 μHz.

2.6.1 ADIPACK

A convincing validation of the model is an independent theoretical computation of the resonant modes followed by a comparison with the simulation. ADIPACK (Christensen-Dalsgaard & Berthomieu, 1991) is a software package that may be employed to produce resonant mode data for the spherical shell under investigation. The simulation was performed in a shell that extended from $0.2R_\odot$ to $0.975R_\odot$ with a transmitting lower boundary and a radially oscillating upper boundary. The eigenfrequencies for this simulation were extracted and compared with results from ADIPACK for a similar model. The comparison result in Figure 2.9, displays good agreement between the ADIPACK modes and the simulation.

2.6.2 Shifts in frequencies due to rotation

We now discuss the validation of the model in the presence of a background rotation profile. To ensure that these frequency shifts can be observed in a short simulation, we artificially amplify the average solar rotation rate by a factor of 10,

$$\frac{\Omega}{2\pi}(r,\theta,\phi) = 4300 \text{ nHz.} \tag{2.23}$$

In the absence of background flows, resonant wave-mode frequencies are characterized only by l, possessing no dependence on m. In general, flows induce changes in the resonant frequencies and specifically, rotation splits the mode frequencies by $\pm m\Omega$, where m is the azimuthal order, depending on whether the modes propagate prograde or retrograde with respect to the direction of rotation. We display the frequency shifts for the $l = 52$ set of modes in Figure 2.10. The frequency resolution of this simulation

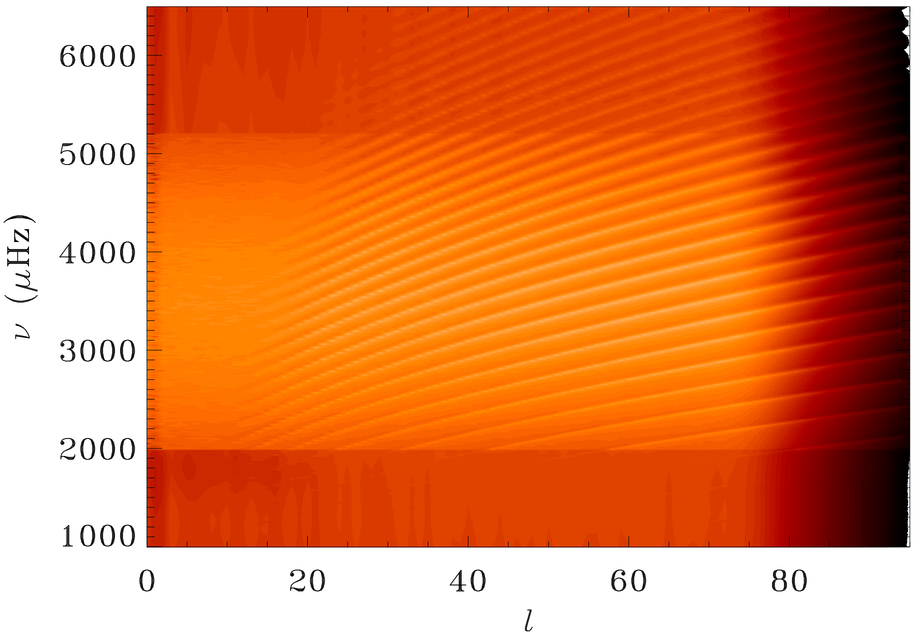

Figure 2.8 Logarithmic power spectrum for a model that extends from $0.24 - 1.00033R_{\odot}$. The excitation spectrum is a band that approximately encompasses $2000 - 5500$ μHz in frequency and $0 - 80$ in l. The highest l's contain little or no power to avoid spatial aliasing. Modes with inner turning points deeper than the lower simulation boundary are absent from this spectrum. Note that because the short time-scale convective instabilities have been removed, as described in §2.5.6, we see no power at frequencies below 2000 μHz. This spectrum was extracted from a 24-hour-long simulation.

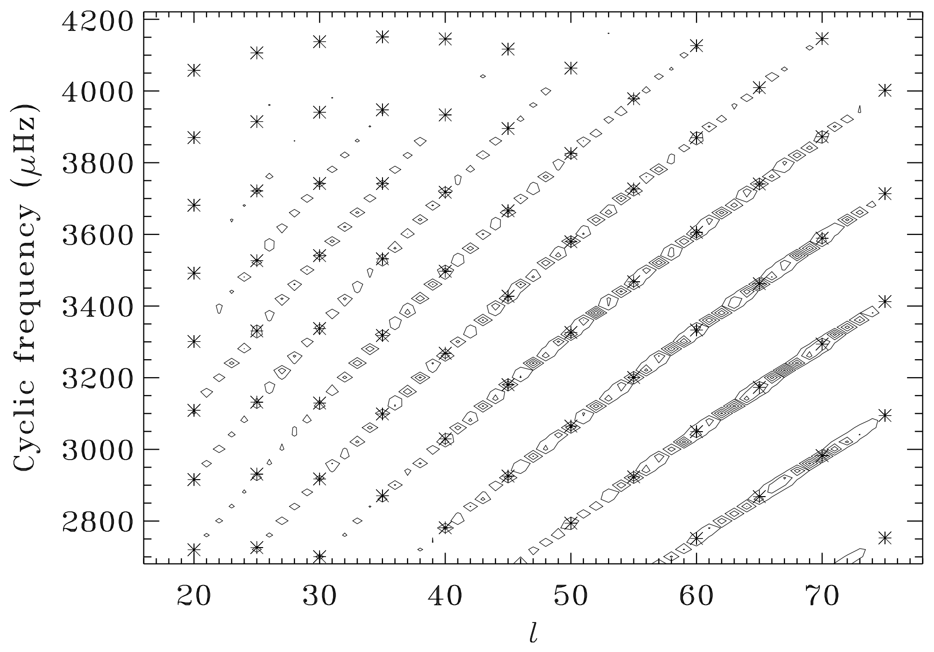

Figure 2.9 Comparison between resonant wave modes computed by ADIPACK and the simulation. The modes extracted from the simulation are depicted as contours of power and the ADIPACK frequencies for this model are shown as stars. Note that for ease of comparison, only one in every five modes that are predicted by ADIPACK are depicted. The mode frequencies, located at contour centers are seen to match closely the frequencies given by ADIPACK. The ridge shapes of the power spectrum extracted from the simulation agree well with those predicted by ADIPACK.

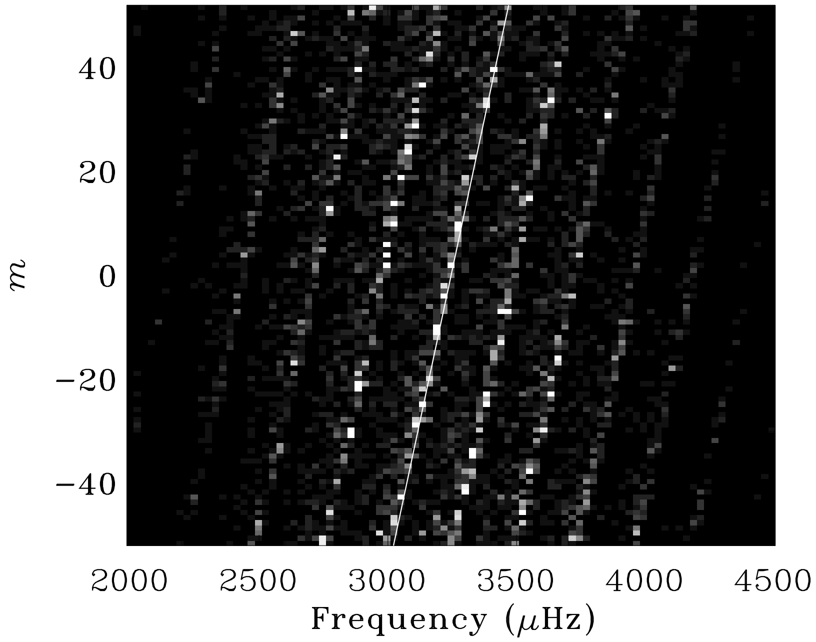

Figure 2.10 The $m - \nu$ power spectrum with $l = 52$ for a simulation with pure rotation, the rate being $\Omega/2\pi = 4300$ nHz. The solid line shows the analytically calculated trend in the frequency shifts. The frequency resolution of this simulation was 28 μHz. In the absence of background flows, contours of maximum power would be lines parallel to the y-axis. Rotation causes frequency splitting, shifting pro-grade modes by $+m\Omega$ and retrograde modes by $-m\Omega$, as indicated by the solid line. Note that as expected, all the (shifted) lines are parallel.

was 28 μHz. The frequency shifts extracted from the simulation match the predicted shifts to within the allowed frequency resolution.

2.7 Results and analyses

2.7.1 Travel times

Using full disk measurements, we were able to extract travel times (see Figure 2.7.1); a comparison between the South pole data (Schrijver et al., 1996) and a simulation datacube is presented. It can be seen that a large fraction of the features are reproduced in the simulation. It is important to note that we do not make a direct comparison between the simulation and actual data since we do not incorporate the full physics in the computation. Also, since the simulation domain extends only down to $r \sim 0.24R_\odot$, we see a phase speed filter like effect that essentially removes the part of the wave-spectrum that penetrates deeper than $0.24R_\odot$. The simulated data shows some ringing effects because the source spectrum in this case is somewhat sharply localized between 2 and 5.5 mHz.

It can also be seen that around the disk edge, the South pole data shows no signal whereas the ridges can be seen clearly right up to the limb in the simulation data. (A)-(C) amongst other ridges (with positive slopes) represent signatures of wave modes that circumnavigate the sun with differing numbers of bounces; several ridges seen in the data are not present in the simulation because these waves propagate deeper than the inner boundary. The ridges (D)-(G) amongst others (with negative slopes) represent wave modes with more complex reflection patterns (some mention of this in Duvall et al., 1993).

2.7.2 Correlations

Figure 2.12 compares time-distance correlations for MDI medium-l data with simulation data. It can be seen that correlations for a given time and distance are approximately the same in both cases. We do not make direct comparisons between the two datasets because we use an altered model of the Sun in simulations. It is interesting to note that the values of the correlation coefficients are comparable. This indicates that the source excitation model we apply is representative of the solar acoustic excitation mechanism in this range of wave-numbers.

2.7.3 Line Asymmetry

Power spectra of the Sun are obtained either through measurements of fluctuations in velocity or in intensity. Mode shapes and line asymmetries in the $l-\nu$ power spectrum are a strong function of source depth (e.g. Rast & Bogdan 1998), with velocity and

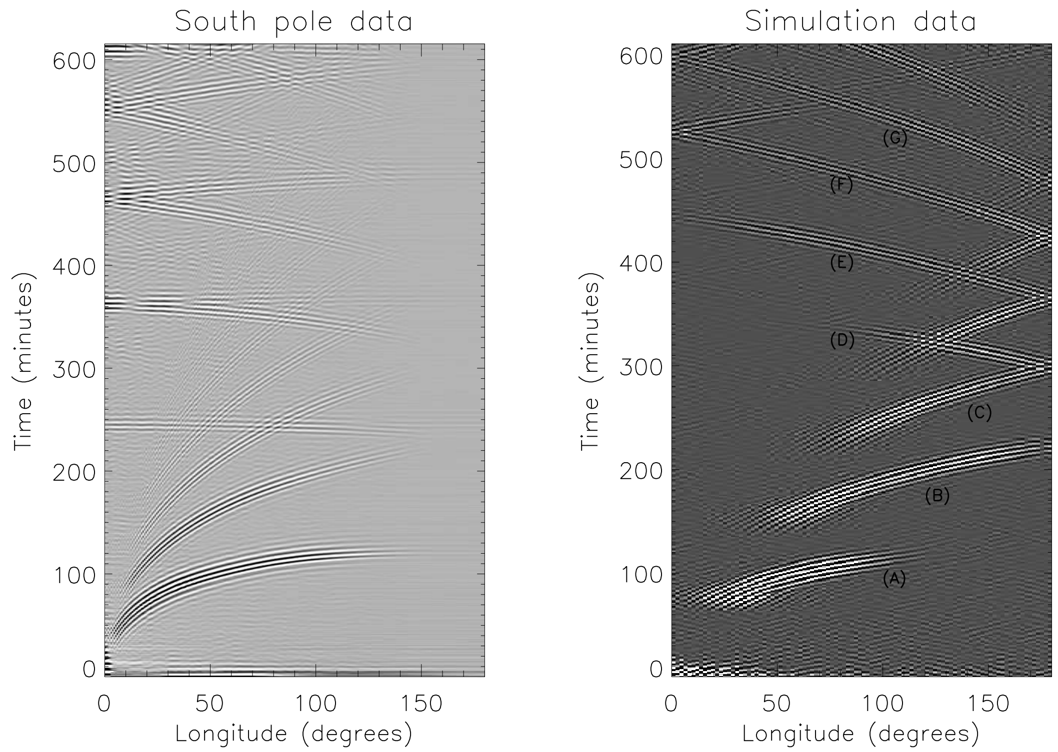

Figure 2.11 Comparison of various ridges obtained from South pole (data first described in Schrijver et al., 1996) and simulated data.

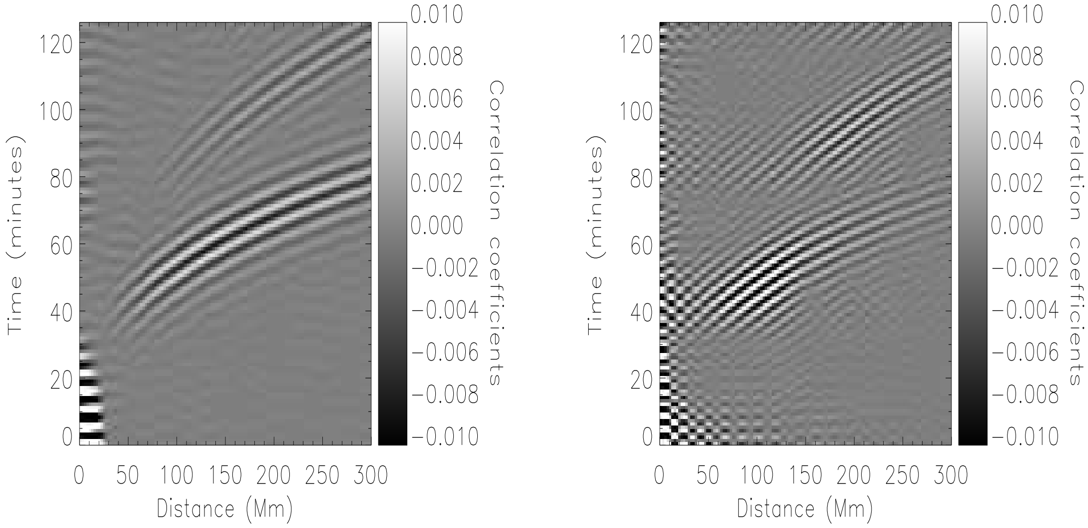

Figure 2.12 Displayed are correlations obtained from MDI Medium-l data on the left panel and simulation data on the right panel. The x-axis is distance in Mega-meters, the y-axis time in minutes and the scale corresponds to the correlation coefficient.

intensity lines displaying phase differences in the asymmetries. By choosing to place sources very close to the surface, we obtain velocity line asymmetries similar to those seen in the Sun, higher on the low frequency side of the mode. By assuming a direct correlation between temperature and intensity fluctuations, Rast & Bogdan (1998) have demonstrated that purely adiabatic oscillations (as in our simulations) result in identical intensity and velocity line asymmetries. An artefact of the simplicity of our adiabatic model and in direct contrast to the Sun, we also observe no phase difference between velocity and intensity asymmetries (figure 2.13).

2.8 Detectability of interior convection

Many investigators have attempted to detect deep convection (e.g., Zhao & Kosovichev, 2004), with some efforts focused on isolating giant cell signatures (e.g., Beck, Duvall and Scherrer, 1998) from solar data. Despite these efforts, giant cells have

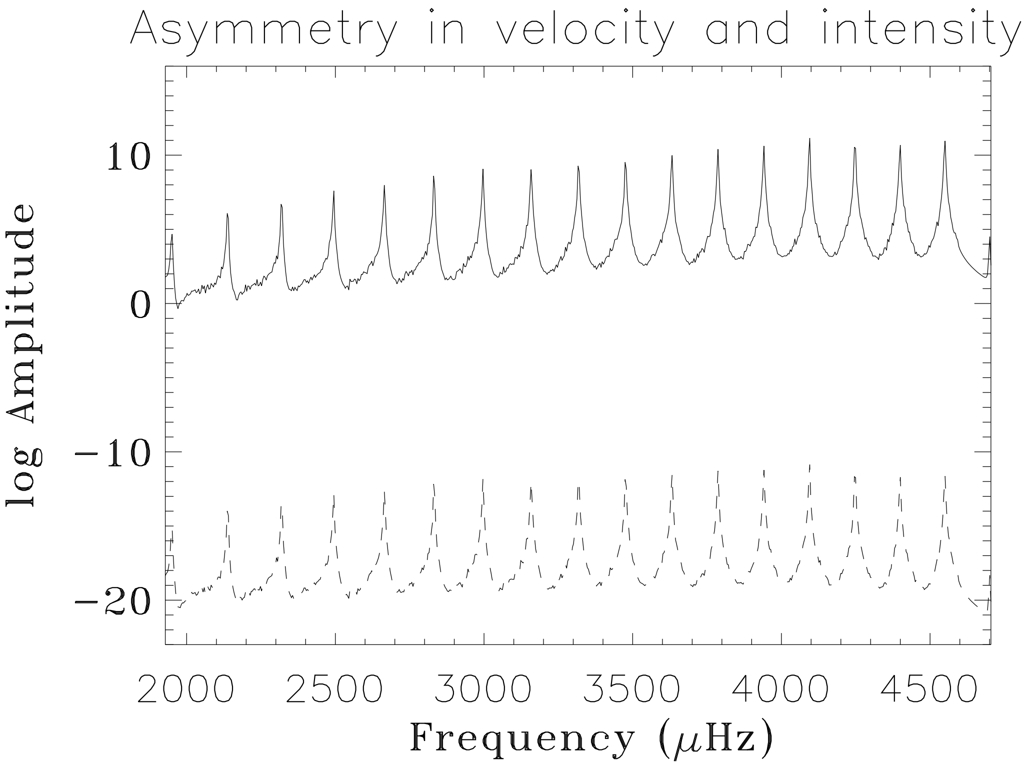

Figure 2.13 Line asymmetry for wave modes with spherical harmonic degree $l = 30$. The mode amplitude is expressed in arbitrary units. The solid line shows modes captured in the velocity spectrum and the dashed line shows modes in intensity (essentially temperature fluctuations). These lines are asymmetric at low frequencies (< 4000 μHz) and become more symmetric as frequency increases (~ 4200 μHz).

not been observed, perhaps due to the relatively small surface velocities they are estimated to possess (e.g., van Ballegooijen, 1985). Furthermore, there have been no convincing observations relating to sub-surface convective activity below the supergranular layer. Swisdak & Zweibel (1999) have shown that solar eigenfrequency shifts may also be poor diagnostic agents because of their weak sensitivity to large scale convection, the effects of which appear only at the second order.

We show in this paper that time-distance helioseismology (Duvall et al., 1993) applied to extract signatures of deep convection may prove to be a promising technique. Time-distance helioseismology is based on measuring wave travel times from one surface location to another to investigate properties along the wave propagation pathways between these locations. In rough summary, signals at these two regions are cross-correlated and analyzed to recover the wave travel times. There are two principal diagnostic agents, the mean travel time and the travel-time difference, the former being predominantly sensitive to sound-speed perturbations and the latter to flows.

It is known that very small thermal perturbations are sufficient to sustain deep convective activity. Convective velocities in the interior, estimated from simulations and otherwise, are placed at 100 ms^{-1}, which in terms of travel-time shifts is arguably a stronger effect than sound speed fluctuations, a direct effect of the convection induced thermal fluctuations. Keeping this in mind, we analyze only travel-time differences, which are sensitive to flows. In order to estimate these travel-time differences, we perform a calculation of a ray propagating through a model of solar convection, taken from the Anelastic Spherical Harmonic (ASH) code (Miesch et. al., 2000). Such a calculation also shows us the correlation between the travel-time maps and the convective velocities that the ray samples.

2.9 Ray calculations

To compute travel-time differences, $\delta\tau$, we use a standard method (e.g., Giles, 2000) that applies the following equation:

$$\delta\tau = 2\left[\int_{r_1}^{r_2} \frac{u_h}{c^2}\left(\frac{\omega^2 r^2}{l(l+1)} - c^2\right)^{-\frac{1}{2}} dr + \int_{r_1}^{r_2} \frac{u_r}{c^2} dr\right], \tag{2.24}$$

where r is the radius, u_h is the horizontal flow velocity component in the direction of the propagating ray, u_r is the radial velocity component along the ray path, ω the circular frequency of the acoustic wave, l the spherical harmonic order, c the sound speed, r_1 the lower turning point and r_2 is the upper turning point. For calculations presented here, we approximate $r_2/R_\odot = 1$. The first and second terms on the right-hand-side denote travel time contributions from the horizontal and radial components of the flow, respectively.

2.9.1 Deep convection model

The ASH code computes acoustics-free convection in a spherical shell. By neglecting the rapidly propagating acoustic waves in the convection zone, Miesch et. al. (2000) are able to obtain a significant increase in the computational timestep of the convection simulation. For the ASH profile used in the ray calculation, the computational boundaries were placed at $0.76R_\odot$ and $0.96R_\odot$ and act as no-slip, impenetrable walls. Because of these boundary conditions, the radial velocity vanishes at both ends and it is important to keep this aspect in mind while interpreting the results from the ray calculations. The latitudinal velocity at a radial layer from the ASH simulation is shown on the upper panel of figure 2.14.

2.9.2 Surface convection model

Acoustic waves spend the longest time in the near-surface layers. These waves are strongly biased by supergranular activity in the sub-photospheric regions. In order to take this effect in account, we model supergranules by cell-like structures with

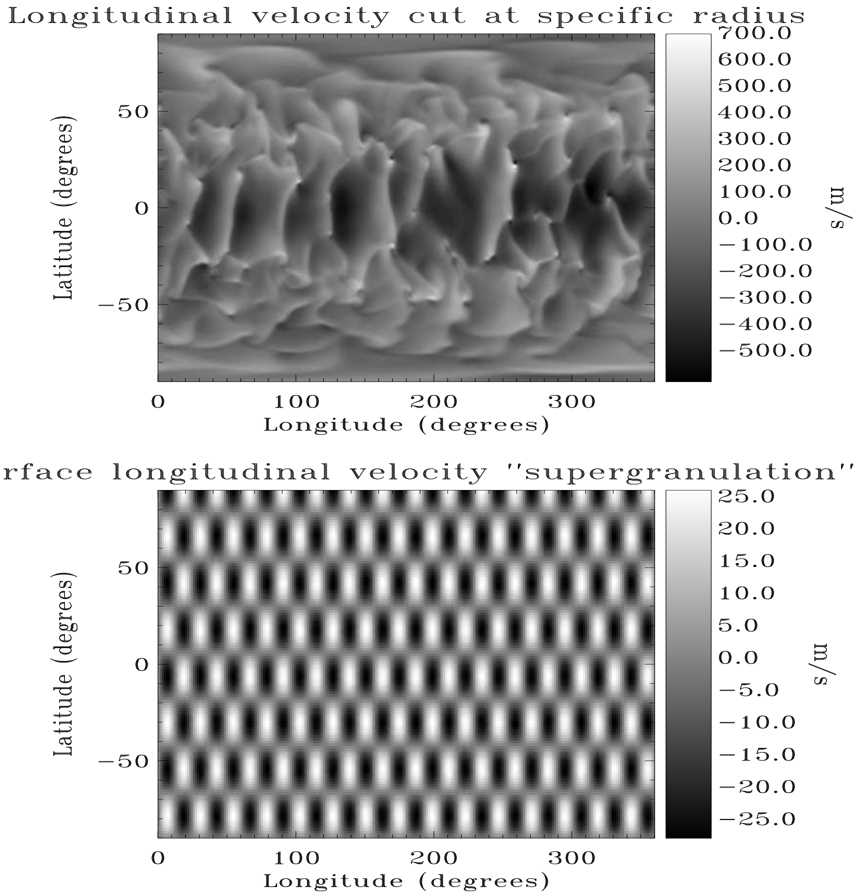

Figure 2.14 Sections of velocity profiles, dimensions of the scale are in m/s. The upper panel shows the longitudinal velocity taken from the ASH simulation at a single radial cut, corresponding to $r = 0.92R_{\odot}$. The lower panel shows the cellular pattern exhibited by the longitudinal velocity at the surface, a crude model for supergranular activity. We use 4 times as many 'supergranules' in our calculations.

an average horizontal cellular size of 30 Mm and depth of 15 Mm. Each unit acts a 'convective cell', with velocity profiles chosen to satisfy the continuity equation, $\boldsymbol{\nabla} \cdot (\rho_0 \mathbf{v}) = 0$ (e.g., Swisdak & Zweibel, 1999), where ρ_0 is the solar density, $\mathbf{v}$ the vector velocity and $\boldsymbol{\nabla}\cdot$ the divergence operator. The maximum velocity of a 'supergranular' cell is 200 ms^{-1}. The surface velocity profile is shown in figure 2.14.

For these calculations, we have taken a snapshot in time from the ASH simulation and apply a constant (in time) surface convection model. One of the reasons we may do this is the decoupling of timescales between the acoustics (5 minutes) and the turnover time of convective cells (several hours to days). Also the long convective cell lifetimes in comparison to the length of the time series of solar data we use to recover the travel-time differences, allows us to invoke the assumption of time constancy.

2.9.3 Travel times

To determine the travel-time difference associated with a point at a certain depth, we first center an annulus around the surface projection of the desired point. The diameter of the annulus is equal to the horizontal distance traversed by a wave whose inner turning point is r_1, as described in equation (2.24). As shown in figure 2.15, we then divide the annulus into 4 equal quadrants, two horizontal quadrants ($[2\pi - \pi/4, 2\pi) \cup [0, \pi/4)$ and $(3\pi/4,\ 5\pi/4]$), and two vertical quadrants ($[\pi/4, 3\pi/4]$ and $(5\pi/4, 2\pi - \pi/4)$). The travel-time differences are divided into two categories, east-west and north-south, based on whether the corresponding rays lie in the horizontal or vertical quadrants, respectively. All the east-west travel times are averaged to give a mean east-west travel-time difference. A similar procedure is implemented for the north-south travel-time difference. When dealing with solar data, this procedure helps in reducing the noise.

We use multiple rays with identical frequencies $\omega/2\pi = 3.2$ mHz but differing inner turning points. For a fixed ω, the inner turning point moves closer to the surface as the degree l increases. In figure 2.16, we show a sample east-west travel-time map for a ray with $l = 128$. On the left panel in figure 2.17, we show the dependence of the RMS travel times (east-west and north-south) with the inner turning point of the

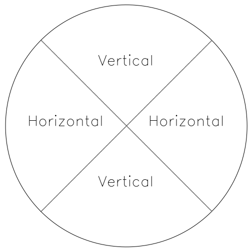

Figure 2.15 Quadrants used for travel time averaging. East-west rays are defined as those which propagate to from one horizontal quadrant to the other. Similarly, rays that span the vertical quadrants are north-south propagating. After computing the travel times for rays propagating in various directions, they are then averaged and classified according to the quadrant in which they propagate.

ray.

RMS travel time differences are shown on the left panel in figure 2.17. The horizontal co-ordinate represents the inner turning point of the ray used to recover these travel times. In general, one may expect that as the coherence of velocity map decreases, i.e. the velocity power is spread over a large range of wave-numbers, travel-time differences and correlations will also decrease. As can be seen in figure 2.18, the longitudinal velocity power peaks at very low l and decays rapidly with increasing l, while the latitudinal velocity power decays more slowly. The greater clustering of power in the convective longitudinal velocity than in latitudinal velocities may be the cause of relatively weaker scattering of waves propagating in the longitudinal direction, possibly leading to the differences in east-west and north-south travel times. Furthermore, it may be seen from figure 2.19 that the longitudinal velocity is consistently larger than latitudinal velocity over the simulation domain, contributing to the larger magnitudes of east-west travel-time differences.

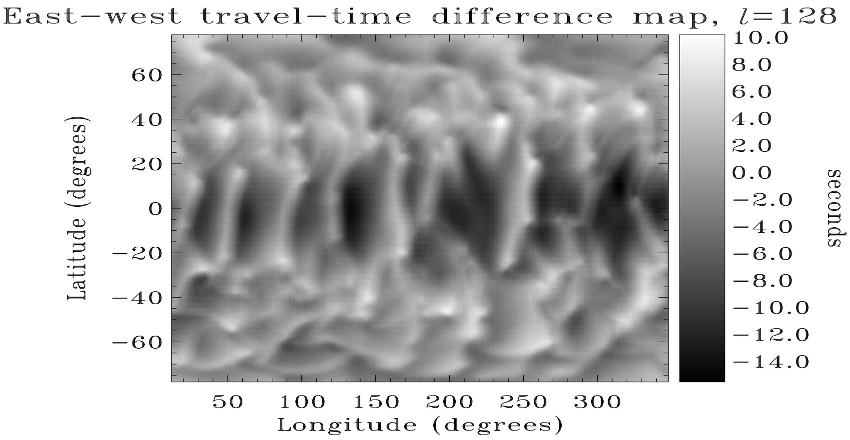

Figure 2.16 East-west travel-time difference map for a ray with $\omega/2\pi = 3.2$ mHz and $l = 128$ (inner turning point $r_1 = 0.92R_\odot$). The correlation of the travel-time map with the longitudinal velocity map (see figure 2.14) at the inner turning point radius is around 0.95, indicating that convective signals are strongly imprinted onto the travel-time differences.

2.9.4 Correlations

The east-west and north-south travel-time difference maps are then correlated with the longitudinal and latitudinal velocity maps at the lower turning point of the ray in question. Correlations as a function of the inner turning point of the ray are shown on the left panel in figure 2.17. The correlations decrease as rays with deeper inner turning points are used. It must be noted that the east-west correlations are not always larger than the north-south correlations, as was the case with RMS travel-time differences (see left panel, figure 2.17). It is interesting to note that the correlation of the shallow rays is very high, perhaps indicating that the convective signals are so well preserved in the travel times that inversions are not needed to recover convective structures at this depth.

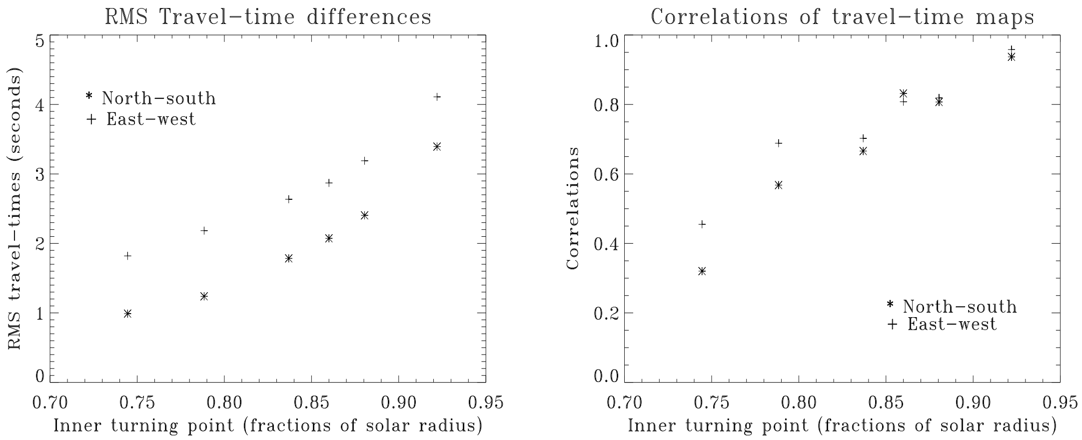

Figure 2.17 The RMS east-west and north-south travel times on the left panel and correlations with corresponding velocity maps on the right panel, as a function of the inner turning point of the diagnostic ray. It can be seen that the east-west RMS travel times are consistently larger than the north-south travel times for a given ray, sometimes by as much as a factor of 2. The correlations do not follow such a clear pattern though.

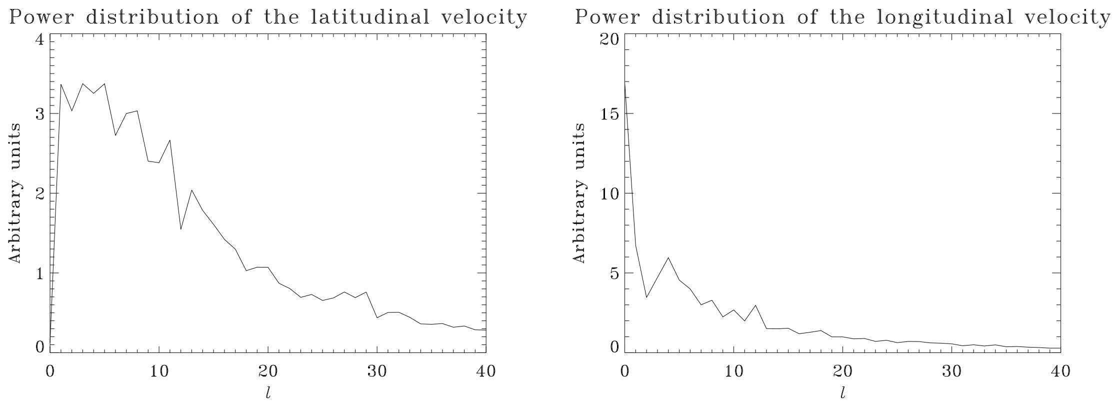

Figure 2.18 Average power of convective velocities from the ASH simulation (in arbitrary units) for each degree, l at $r = 0.92R_{\odot}$. While the power increases from the bottom of the domain to the top, the distribution profile is almost constant with radius. The variation of power with wavenumber indicates the extent of the scattering caused by the convection on the propagating rays. The longitudinal velocity power is strongly focused around $l = 1$, indicating that the travel times will preserve the velocity structure of the convection.

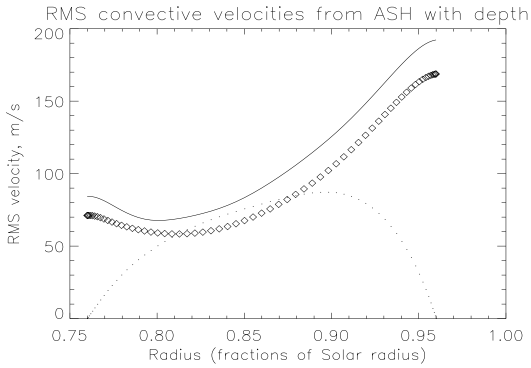

Figure 2.19 RMS convective radial, latitudinal and longitudinal velocities from the ASH simulation, as a function of depth. The solid line shows the longitudinal RMS velocity, the dots show radial velocity and the symbols depict the latitudinal RMS velocity.

2.10 Summary and Conclusions

A method to perform *differential* studies of the effects of flows and asphericities on the acoustic wavefield in full spherical geometry has been proposed. We have designed a technique to attempt the *forward* problem of helioseismology by performing linear acoustic simulations in an appropriately perturbed solar-like spherical shell. The utility of developing a means to independently test the ability of a helioseismic technique to probe various interior phenomena cannot be understated. From a practical standpoint, this technique is useful in understanding signatures of large scale phenomena such as meridional flow or the tachocline, and important in calibrating techniques that depend inherently on the geometry being spherical. Moreover, various systematics such as center to limb travel-time variations and fore-shortening can be investigated, given the availability of vector velocities and a 360^o view of the sphere.

In the past, there have been tests of helioseismology (for example, see Jensen et al., 2003) that have involved computations of acoustic wavefields but none have been performed in spherical geometry. From a practical standpoint, this technique is useful in understanding signatures of large scale phenomena such as meridional flows or the tachocline, and important in calibrating techniques that depend inherently on the geometry being spherical. Moreover, various systematics such as center to limb travel-time variations and fore-shortening can be investigated, given the availability of vector velocities and a 360^o view of the sphere.

We have discussed some of the issues associated with a computation of this kind, methods to overcome them and various techniques used in the validation process. The presence of a varying background medium introduces several complications that affect the stability and accuracy of the calculation. For example, the choice of an appropriate radial grid is somewhat crucial to the accuracy of the calculations given a motivation to minimize computational cost. Wave propagation in a such a medium is quite different in comparison to media that traditional aero-acoustic computations are accustomed to. Of course, the side-effects of a changing base state can ease and hinder the computation as has been noted.

We have demonstrated a way of filtering out waves based on their inner turning points, a technique of avoiding tight CFL restrictions and of circumventing instabilities created by an unstable background model. Important to a calculation of this kind is the need to validate the results. We have shown the utility of the process of extracting resonant modes of the domain and techniques to calculate the modes theoretically. The theoretical calculations confirmed the results of the numerical computation.

Observing interior convection in the Sun is a very exciting prospect. If we are indeed able to observe these convective cells, even if they are relatively close to the surface, we will be able to understand if current models accurately predict the characteristic sizes of these cells and the associated convective velocities. If we are to believe that the ASH simulations are representative of the solar convection zone, then from the results we obtain, convective signals are strongly imprinted onto the travel-time difference maps. The correlations we obtain in the near-surface regions are so high (~ 0.95) that inversions are not necessary to recover the structure of convection at this depth. In terms of real data, we will extract travel times using the deep-focusing technique described in Duvall (2003).